
Article:
Malekabadi, Fatemeh, Caldag, Hakan Osman orcid.org/0000-0002-4394-6045 and Yesilyurt, Serhat (2023) Acoustic radiation forces and torques on elastic micro rings in standing waves. Journal of Fluids and Structures. 103841. ISSN: 0889-9746

https://doi.org/10.1016/j.jfluidstructs.2023.103841

Acoustic Radiation Forces and Torques on Elastic Micro Rings in Standing Waves

Fatemeh Malekabadi[1], Hakan Osman Caldag[2], Serhat Yesilyurt[1]
[1]Mechatronics Program, Sabanci University, Istanbul, Turkey
[2]Department of Mathematics, University of York, York, UK

Abstract

Acoustic radiation forces and torques are very effective in manipulating micron-sized objects such as cells, droplets, particles, and organisms. In this work, we present analysis of acoustic radiation forces and torques on ring-shaped slender microstructures under a standing wave in an inviscid fluid using on a three-dimensional finite-element-method (FEM) model. The influence of geometric and physical parameters on the radiation forces and torques is characterized. The radiation force tends to push the rings towards the pressure nodes or anti-nodes depending on the contrast factor and exhibits a volumetric dependence in magnitude on geometric parameters. Moreover, a nonzero net torque develops when the ring is not co-planar with plane waves and varies in magnitude and direction depending on the position, orientation, and material properties of the ring. Large variations are observed only in torque values for specific combinations of geometric and physical parameters as an indicative of resonance. Furthermore, the FEM results are compared with a reduced-order model called chain-of-spheres, which works well in estimating the radiation forces at a fraction of the computational cost but deviates significantly in torque evaluations. Lastly, a segmented ring is used to understand the relative effect of secondary forces due to self-scattering. The findings of the study are applicable to development of acoustic manipulation systems for ring-like elastic microfilaments and slender bodies with arbitrary shapes and orientations. These results also can be used in directional reinforcing of ring-shaped composites.

Keywords: micro rings; acoustic radiation force; acoustic radiation torque; elastic microfilament loops; self-scattering effects; resonance

1. Introduction

Ultrasound waves in microfluidic devices provide versatile control for manipulation of microparticles such as cells [1-4], droplets and bubbles [5-6], particles [7-9], organisms [10,11] and colloids by means of acoustic radiation forces (ARF), which result from the second-order pressure and momentum flux acting on a particle's surface in an inviscid fluid [12-18]. In the literature, ARF on simple structures such as spheres and cylinders have been studied extensively. King [19] was the first to study the acoustic radiation force on incompressible spherical particles in an inviscid fluid in both plane progressive and standing waves. Yosioka and Kawasima extended King's study to compressible spheres [20] and Gor'kov [21] proposed a generalized potential for the calculation of the ARF for a wide range of applications in inviscid fluids. Hasegawa and Yosioka [22] and Hasegawa [23] reported simple analytical formulae for the ARF under travelling and standing acoustic waves, respectively. Moreover, in [14,17,18] viscous effects are considered, and thermal effects on the acoustic radiation force have been

studied extensively in [24-27]. ARF on spheroidal objects under arbitrary acoustic fields are studied in [28-32]. The acoustic pressure on disks was also modeled by King [33] and the theory was developed further for the forces on disks [34], deformed droplets [35], cylinders [36-39], and ellipsoids [40]. Later, experimental studies investigated the ARF for the entrapment of cylindrical particles [41].

Despite a wide range of studies utilizing analytical solutions for the ARF, numerical methods are necessary to solve the problem without overbearing simplifications on the properties of the fluid and the particle. The numerical studies can be classified under two broad categories. The first one approaches the problem as a fluid mechanics problem and the acoustic field is introduced as a flow field. Wang and Dual's [39] finite volume method-based approach to calculate the acoustic radiation forces on cylinders utilizes such an approach. Their results match very well with the analytical calculations but solving for the whole flow field using the Navier-Stokes equations is computationally very expensive. Such an approach is not feasible especially if one is only concerned with the radiation force computation. Grinenko et al [42] calculated the acoustic radiation force directly from nonlinear governing equations using a finite-difference time-domain method based on the Lagrangian specification of the flow field; the method does not have any limitation on particle geometry and any overly constraining boundary condition. Wijaya et al [43-44] analyzed the acoustic radiation forces and torques on spherical and non-spherical particles using the boundary-element method.

In the second category, the Helmholtz's equation is solved by using perturbation methods for the time-harmonic acoustic field, velocity, and the density of the fluid. Using this approach, Glynne-Jones et al. [16] (for an inviscid fluid) and Baasch et al [15] (for a viscous fluid) calculated the ARF on a spherical particle under a standing acoustic field. Both methods take advantage of the spherical symmetry using a two-dimensional axisymmetric geometry, cutting the computational costs even further. Garbin et al. [45] propose a three-dimensional finite-element model to compute the forces and torques on disk-shaped particles. Their cubic fluid domain is surrounded by perfectly matched layers (PML) to prevent the reflection of outgoing waves but it is observed in the literature that proper radiation boundary conditions work just as well as PMLs while reducing the computational cost [16,12].

Perturbation-based methods are computationally more efficient, but they may remain costly especially for complex three-dimensional structures, such as helices, at high acoustic frequencies where the resolution of the acoustic field is more demanding. Recently, Caldag & Yesilyurt [12] introduced a reduced-order model called chain-of-spheres (CoS) to calculate the

acoustic radiation forces on slender objects in inviscid fluids by approximating the slender structure as a chain of small spheres, each having the same volume as the corresponding segment of the slender body. The total radiation force on the slender structure is evaluated from the sum of the individual forces acting on small spheres, which are calculated analytically either from [22] or [23] depending on the incident acoustic wave. The approach is extremely efficient computationally and fairly accurate in comparison to the results obtained from the direct numerical solution of the total acoustic field.

Acoustic manipulation is an extremely versatile method for handling of micro/nano particles of various shapes such as spheres, spheroids, disks and cylinders [46,47]. Yet, despite being a common topological structure in the microcosm, acoustic radiation forces and, especially, torques on three-dimensional slender structures, such as rings have not received much attention so far. Especially biopolymers forming loops by knots and entanglements are ubiquitous structures that play important biological functions [48] and acoustic manipulation may be effective in studying them. Microrings are also used as mechanical sensors [49] and in nonlinear optics [50] as well. Ring-shaped structures have also attracted interest in cell-patterning by acoustic fields that have potential applications in *in vitro* vascularization [51]. Moreover, bulk acoustic waves are used to align carbon nanotubes for reinforcing composite materials [52].

This work reports forces and torques on slender micro rings, to the best of authors' knowledge first time, based on a finite-element model with a comprehensive analysis of the effects of position, orientation, geometrical and physical parameters of rings. According to simulation results, forces scale with the volume of rings and very similar to forces on spheres having the same volume, whereas the torques are mainly restorative in nature with respect to planar waves and depend strongly on physical properties; in particular, torque drops to a minimum at a low, positive acoustophoretic contrast factor. Moreover, effects of resonances are observed at certain geometries leading to very large variations in torque trends. Furthermore, we use the CoS approach [12], as a reduced-order model, for comparisons with computationally more expensive FEM simulations. Whilst the CoS method is very accurate for force comparisons, torque results vary greatly as the CoS cannot account for the elastic behavior of the slender structure. Lastly, a segmented ring structure is used to identify the conditions where self-scattering forces become important on the local force distribution and, hence, the torque acting on the ring.

2. Methodology

2.1 The Calculation of the Acoustic Radiation Force and Torque

For the calculation of the ARF on slender rings in fluids, we use linearized inviscid compressible Navier-Stokes equations as adopted commonly in literature, e.g. [12-13]. Thermal effects are neglected, meaning that the density only depends on the pressure, p. The fluid is assumed to be inviscid. The perturbation method is used to expand the physical fields in series:

$$\rho = \rho_0 + \rho_1 + \rho_2 + \cdots \tag{1}$$

$$p = p_0 + c_a^2\rho_1 + p_2 + \cdots \tag{2}$$

$$\boldsymbol{v} = 0 + \boldsymbol{v}_1 + \boldsymbol{v}_2 + \cdots \tag{3}$$

where ρ and p are the fluid density and pressure, respectively and v corresponds to the velocity vector and c_a is the speed of sound inside the fluid. The subscripts in the terms indicate the order of the terms, with the subscript 0 indicating the values in a quiescent fluid, that is why $v_0 = 0$. Assuming that all the fields inside the fluid are time-harmonic in the first-order, one can write:

$$\rho_1(r,t) = \rho_1(r)e^{-i\omega t} \tag{4}$$

$$p_1(r,t) = c_0^2\rho_1(r)e^{-i\omega t} \tag{5}$$

$$\boldsymbol{v}_1(r,t) = \boldsymbol{v}_1 e^{-i\omega t} \tag{6}$$

where $\omega = 2\pi f$ is the angular velocity of the acoustic field, f is the frequency, and t is time; hence, the acoustic wavelength is defined as $\lambda = c_0/f$.

Inserting the first-order perturbed fields into the governing equations, leads to first-order continuity and inviscid Navier Stokes equations [13]:

$$\partial_t\rho_1 = -\rho_0\nabla\cdot\boldsymbol{v}_1 \tag{7}$$

$$\rho_0\partial_t\boldsymbol{v}_1 = -c_0^2\nabla\rho_1 \tag{8}$$

The subscript "t" in the expressions indicates the time derivative. Substitution of the second-order expansions into Eqs. (7) and (8), the time-averaged second-order continuity and inviscid Navier Stokes equations become:

$$\rho_0\nabla\cdot\langle\boldsymbol{v}_2\rangle = -\nabla\cdot\langle\rho_1\boldsymbol{v}_1\rangle \tag{9}$$

$$-\nabla\langle p_2\rangle = \langle\rho_1\partial_t\boldsymbol{v}_1\rangle + \rho_0\langle(\boldsymbol{v}_1\cdot\nabla)\boldsymbol{v}_1\rangle \tag{10}$$

For an inviscid fluid, the time-averaged acoustic radiation force (up to second order) can be calculated via an integration over a fixed surface enclosing the ring, S_0 [16]:

$$\boldsymbol{F}^{rad} = -\int_{S_0} \langle p_2 \boldsymbol{n} + \rho_0 (\boldsymbol{n} \cdot \boldsymbol{v}_1) \boldsymbol{v}_1 \rangle dS \tag{11}$$

where $\mathbf{n}$ is the outward normal vector of the surface and "$\langle\ \ \rangle$" indicates the time average over a complete period, and the time-averaged second order acoustic pressure is given by

$$\langle p_2 \rangle = \left(\frac{1}{2\rho_0 c_0^2} \langle p_1^2 \rangle - \frac{\rho_0}{2} \langle |v_1|^2 \rangle \right) \tag{12}$$

Similarly, the time-averaged acoustic radiation torque is calculated from:

$$\boldsymbol{\tau}^{rad} = -\int_{S_0} (\mathbf{r} - \mathbf{r}_0) \times \langle p_2 \boldsymbol{n} + \rho_0 (\boldsymbol{n} \cdot \boldsymbol{v}_1) \boldsymbol{v}_1 \rangle dS \tag{13}$$

where $\mathbf{r}$ denotes the coordinates of a point on the surface, S_0, and $\mathbf{r}_0$ denotes the center-of-mass of the ring.

2.2 The Finite-Element Model

Analytical calculation of forces and torques over a ring or torus in plane acoustic fields is extremely difficult especially in the case of a tilted ring with respect to the plane of propagation. Hence, we use the finite-element method, which is reliable to use for linear problems and capable of modeling complex three-dimensional structures such as rings. As sketched in FIG 1, an elastic ring of major radius R and the minor radius a is rotated around the y-axis by angle θ and placed in a fluid domain. The finite-element model of the ring is built in COMSOL Multiphysics software. Assuming a planar background pressure field in the z-direction that represents standing waves, we used time-harmonic formulations in the frequency domain for the pressure amplitude in the fluid and the displacement amplitude in the elastic solid. Acceleration and pressure terms are coupled at the solid-fluid interface and time-averaged forces and torques are obtained from Eqs. 12 and 13 by setting S_0 as the surface of the ring. Planar non-reflection radiation boundary conditions (NRBC) are used to ensure a standing acoustic field without any reflections [55,56]. Planar NRBC is preferred over perfectly matched layers (PML) for computational efficiency as comparisons between NRBC and PML conditions show negligible differences. Moreover, the domain size is much bigger than the ring size to ensure the resolution of the acoustic field properly by keeping the boundaries away from the ring. We compared the

cubic fluid domain with spherical and cylindrical fluid domains and observed no significant difference.

Tables I and II list the values of the physical and geometric parameters used in the simulations. The fluid domain is taken as water, and polystyrene, copper and aluminum rings are simulated to observe the effects of rigidity on the forces and torques.

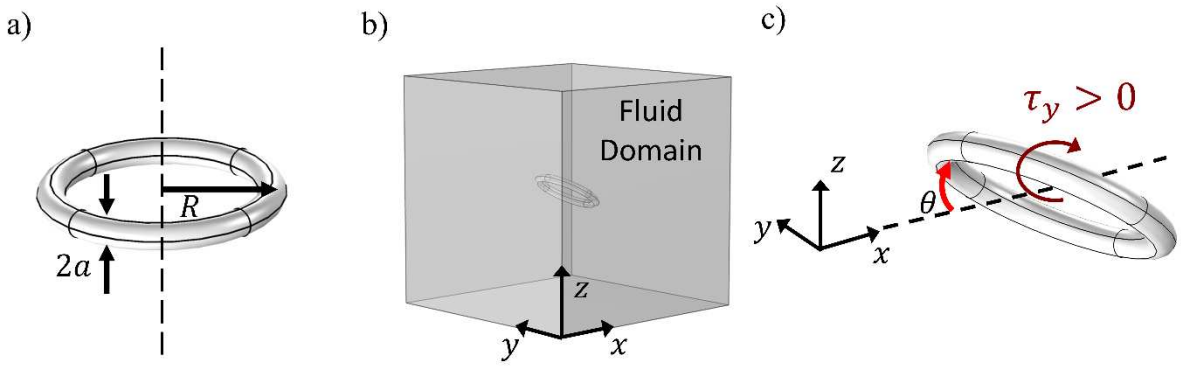

FIG 1. (a) Geometric parameters of the ring. (b) Simulation domain with the ring placed inside a fluidic domain with radiation conditions at the boundaries. (c) Depiction of the ring rotation angle, θ.

TABLE I. Fluid properties and geometric parameters for the reference ring.

Parameter	Symbol	Value	Units
Density	ρ_0	998.2	kg m^{-3}
Compressibility (reciprocal of bulk the modulus)	$\kappa_0 = \frac{1}{K} = \frac{1}{\rho_0 c_0^2}$	4.76×10^{-10}	Pa^{-1}
Fluid speed of sound	c_0	1482	ms^{-1}
Pressure amplitude	p_a	100	kPa
Minor Radius	a	3	μm
Major Radius	R	25	μm

TABLE II. Solid properties of materials and the geometric parameters for the reference ring.

Parameter	Symbol	Polystyrene	Copper	Aluminum	Units
Solid density	ρ_p	1050	8930	2700	kg m^{-3}
Compressibility (reciprocal of the bulk modulus)	$\kappa_p = \frac{1}{K} = \frac{1}{\rho_p c_p^2}$	4.25×10^{-10}	8.26×10^{-12}	1.42×10^{-11}	Pa^{-1}
Longitudinal velocity	c_p	2400	5010	6420	ms^{-1}
Shear velocity	c_s	1150	2270	3040	ms^{-1}

The acoustic field is imposed as a standing wave via background pressure, defined as:

$$p_b = p_a \cos\left(k(z - \Delta z)\right) \tag{14}$$

where z is the axial position along the wave propagation direction, k is the acoustic wavenumber, $k\Delta z$ is the phase angle. At the solid-fluid interface, total pressure from the fluid domain

is specified as a boundary load onto the solid and the acceleration from the solid domain is specified as boundary acceleration onto the fluid.

A mesh convergence study on the finite-element model is carried out over the acoustic radiation force calculated from Eq. (11) with the first-order velocity and second-order pressure fields. $f = 6$ MHz in this study as this is the case with the lowest wavelength in this work, hence the most constraining in terms of mesh element size. It is reported in the literature that the mesh element size [57] should be at least six times smaller than the acoustic wavelength for linear elements and twice smaller for second-order elements in finite-element models of acoustic waves for a proper resolution. Here, key dimensions of the ring are much smaller than the wavelength, hence the convergence mainly depends on the element size on the ring. A relative convergence error e is calculated with respect to calculated forces in the z-direction obtained from the finest mesh:

$$e = \left| \frac{F^{rad} - F^{rad,finest}}{F^{rad,finest}} \right| \tag{15}$$

The results of the convergence study are displayed at FIG 2. The relative error falls below 2% for, $\delta = 0.002 \times \lambda$, which is the maximum element size on the ring surface and corresponds to 1.25×10^6 degrees-of-freedom, which is used for the rest of the simulations reported here.

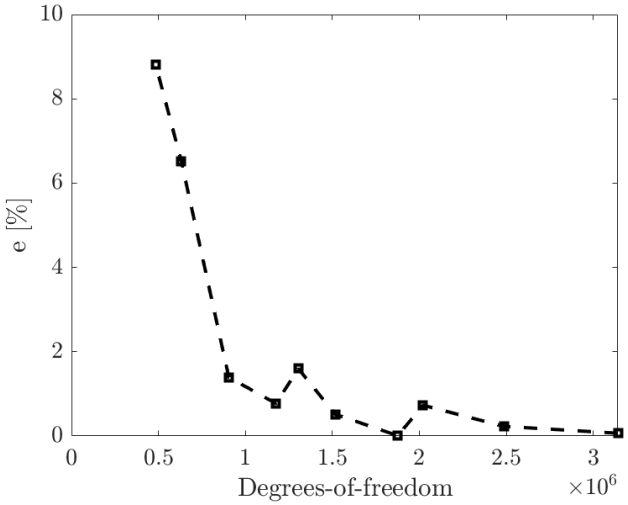

FIG 2. Convergence of F^{rad} with respect to the degrees of freedom.

As there is no previous study that reports the radiation forces on rings, we validate the model by comparing the force values on spheres and cylinders. First, a polystyrene sphere with a radius of 3 μm is placed in a standing acoustic field with $p_a = 100$ kPa and $f = 2$ MHz. The radiation force on a sphere evaluated from Hasegawa's model [23] comes out as 0.576 pN while our 3-

dimensional model gives 0.569 pN. The relative percentile error between the Hasegawa [23] and the FEM model is 1.21, indicating high accuracy. Then, we validate the model by comparing the force values for a copper cylinder of equal length and cross-section as the ring using the geometric and physical parameters in Table I. FIG 3 compares the magnitude of the acoustic force calculated on both structures via Eq. 11. The force values match for a great majority of cases tested, the values begin to diverge only slightly at large a, which corresponds to a ring less reminiscent of a cylinder as $a \to R$.

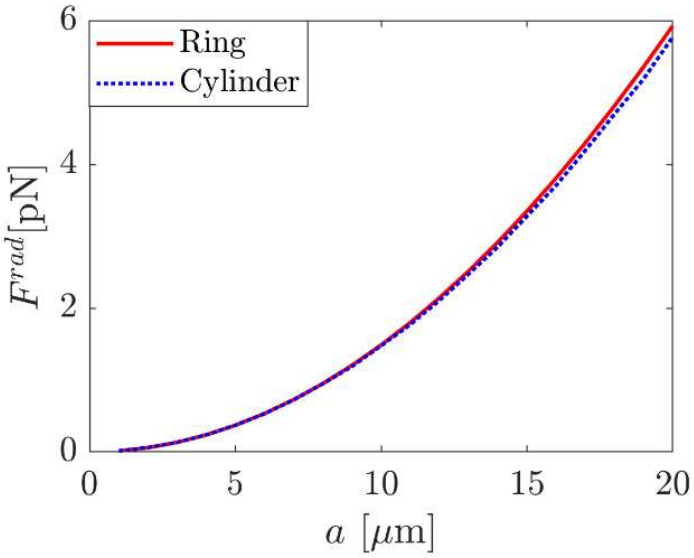

FIG 3. Comparison of the acoustic radiation forces on a ring and cylinder with equal volumes.

3. Results

This section presents the effects of minor and major radii of the ring, its orientation and position with respect to the plane waves and material properties on the acoustic radiation force (ARF) in the z-direction and the acoustic radiation torque (ART) in the y-direction. All the forces and torques are reported in dimensional terms similar to studies in literature [15,16,45]. Nonetheless, Appendix A presents a complete dimensional analysis for the acoustic radiation forces and torques on a ring with the help of analytical solutions for spheres. The analysis is extremely helpful in terms of elucidating the effects of orientation, position, and the geometric parameters of the ring. The baseline geometric parameters in Table I are used for a polystyrene ring in all simulations reported here except indicated otherwise.

3.1 Effects of Position and Orientation

First, we report how the position of the ring relative to the pressure field affects the radiation force and torque. The pressure nodes and values with respect to Δz are shown in FIG 4a and

FIG 4b respectively, and the corresponding F^{rad} profiles for a horizontal ($\theta = 0°$) and rotated ($\theta = 30°$) polystyrene ring are plotted in FIG 4c. Dependence of F^{rad} on the position follows a sine profile as shown in Appendix A. Moreover, the effect of orientation is negligible as the force for a non-rotated ring ($\theta = 0°$) differs only slightly from the values for the rotated ring since $R/\lambda = 0.0337 \ll 1$. Similar to spherical particles, rings located near the pressure nodes, $\Delta z = \lambda/4$, will be driven towards that node, as $F^{rad} > 0$ for $\Delta z < \lambda/4$ and vice versa. Whereas the pressure nodes are not stable since $F^{rad} > 0$ for $\Delta z > \lambda/4$ and vice versa as a ring slightly away from the node will be driven away further. The maximum force is observed when $\Delta z = \lambda/8$, at a distance of $\lambda/8$ away from the pressure node, which is shown in FIG 4a. Acoustic radiation torque on the ring is plotted with respect to position in FIG 4d. As shown in Appendix A (Eq. A8), we see a cosine dependence with respect to the position for the tilted ring with $\theta = 30°$. The torque is negligible when $\theta = 0$.

FIG 5a shows the force values for a wide range of θ for both $\Delta z = 0$ and $\Delta z = \lambda/8$. F^{rad} is near zero when $\Delta z = 0$ as expected, showing that the pressure nodes are stable equilibrium points for the rings similarly to spheres. For $\Delta z = \lambda/8$, F^{rad}varies slightly with respect to θ, the ratio of force values for $\theta = \pi/2$ and 0 is 0.9657. Simple analysis in Appendix A gives $J_0(2kR\sin\theta)$ dependence (Eq. A5) for the force; for $2kR = 0.424$, $J_0(0.424 \times \sin\theta)$ varies between 1 and 0.9556 for $0 < \theta < \pi/2$.

We present the radiation torque values as a surface plot where we vary both Δz and θ in FIG 5b. The torque is, as expected, 0 for $\theta = 0°$ and $\theta = 90°$. For other values, it is mostly restoring, i.e. negative or clockwise in the y-direction (see FIG 1c) at low θ, meaning that the ring would align with the pressure wave on the xy-plane ($\theta = 0$, see FIG 5c). The restoring torque is the strongest when Δz is close to an odd multiple of $\lambda/4$. At large θ values, the torque value becomes positive, i.e. counter-clockwise in the y-direction, meaning that the ring is rotated to align perpendicular to the standing wave ($\theta = 90°$, see FIG 5d). Also notice that there is a region separating positive torque values from the negative values (identified with a solid line in FIG 5b), a crude approximation for the curve separating the two regions is given by $\theta = 62.5 - 27.5\cos\left(\frac{k\Delta z}{2}\right)$. This curve tells that the ring can be rotated and kept at any angle simply by tuning Δz. Another point of interest would be the contributions from the momentum and pressure components to the torque, given at FIG 5e for $\Delta z = 0$. It is observed that the force terms due to pressure and momentum flux, i.e. the first and the second terms in the force calculation in Eq. (11), are acting against each other. The momentum flux component is dominant

at low θ, aligning the ring horizontally whereas at larger θ, pressure-induced torque is dominant, and the ring is rotated into a vertical alignment. Lastly, ART has a mild sinusoidal dependence on the orientation angle, θ, consistently with Eq. A8 in Appendix A.

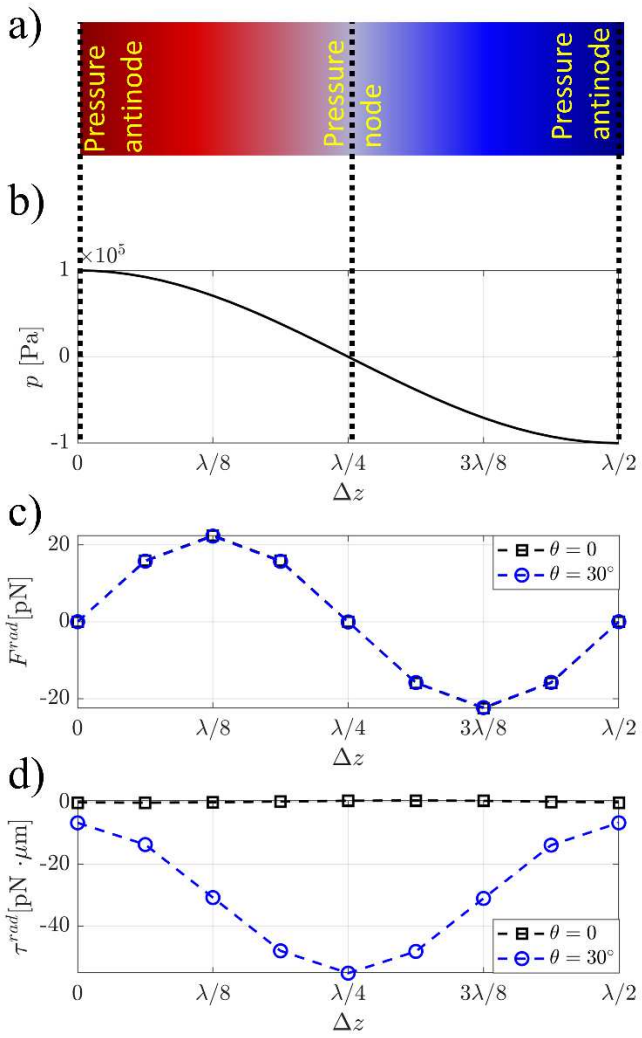

FIG 4. The radiation force and torque with respect to Δz in a standing wave on a horizontal ($\theta = 30°$) and tilted ($\theta = 30°$) polystyrene ring in water for a frequency of 2 MHz (R/$\lambda = 0.0337$). a) Color plot of the pressure amplitude, b) Change of p with respect to Δz and the corresponding c) F^{rad} and d) τ^{rad} profiles.

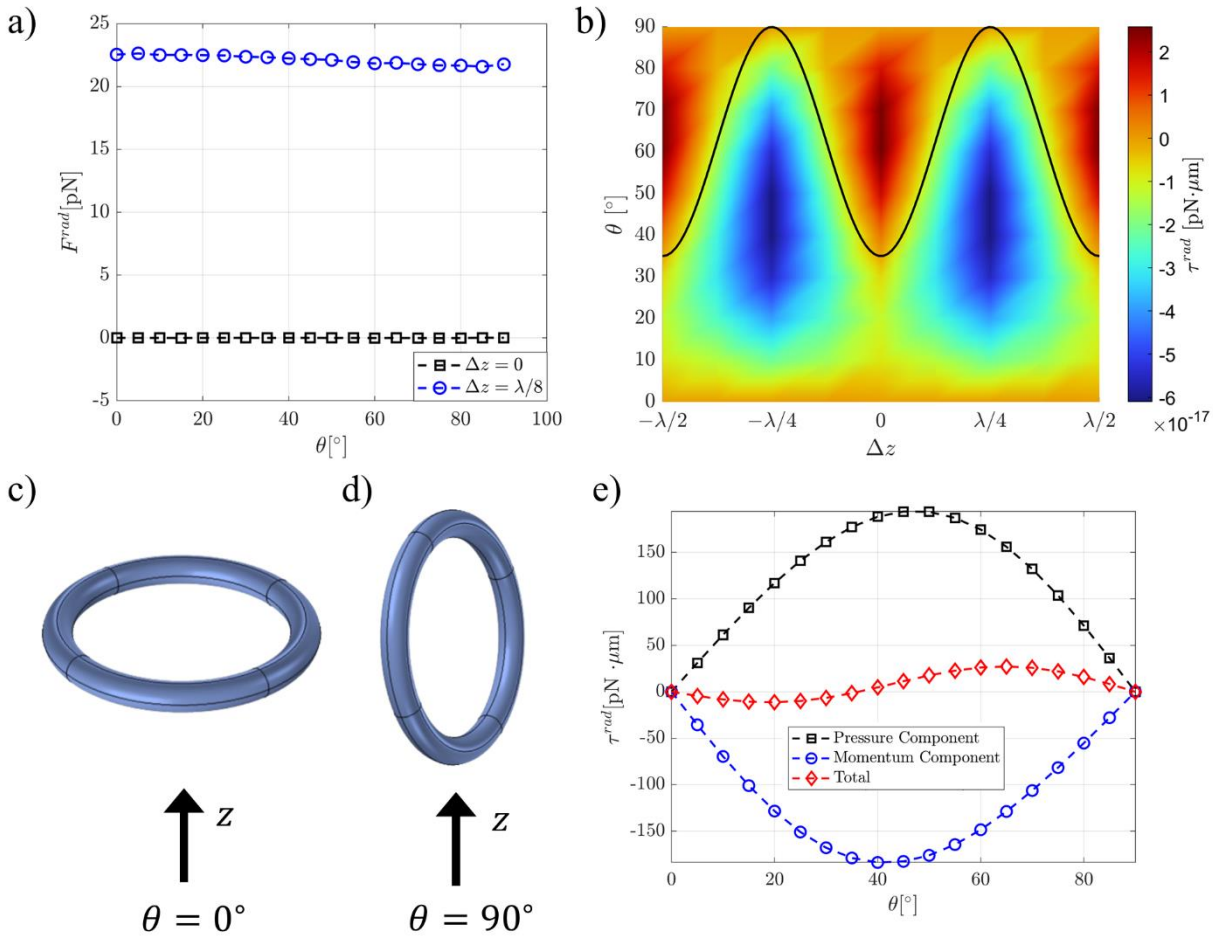

FIG 5. The change of (a) F^{rad} with respect to θ. (b) shows a colormap of τ^{rad} with respect to Δz and θ. The solid line on the plot is the curve with zero torque. (c) shows the ring's orientation when $\theta = 0°$ and (d) shows the orientation when $\theta = 90°$. The standing field is applied in the z- direction. (e) shows the pressure and momentum flux-driven component of the radiation torque on a polystyrene ring when $\Delta z = 0$.

3.2 Effects of Minor and Major Radii

The effects of the ring's minor and major radii on the ARF and ART are plotted at FIG 6. F^{rad} increases quadratically with a in FIG 6a due to the scaling of the force with the volume of the ring. Looking at the corresponding torque values for a rotated ring ($\theta = 30°$), we initially observe a quadratic increase in the magnitude of τ^{rad} with respect to a, but then at $a = 4$ μm the torque value increases more than two times after which it passes through 0 and goes above 500 pN · μm at $a = 4.2$ μm. The change in the geometry leads to a change in the sign of the torque. At low a, the torque is a restoring one that tends to align the ring horizontally ($\theta = 0$). At larger a values, the torque tends to align the ring vertically ($\theta = 90°$). Similarly, increasing the major radius of the ring increases the ARF linearly as the volume of the ring varies linearly with R (FIG 6c) and the torque exhibits a sudden jump (FIG 6d) as observed in FIG 6b. This

time, we see that the radiation force tends to align rings with small R vertically ($\theta = 90°$) while the rings with larger R are rotated towards a horizontal alignment ($\theta = 0°$).

Dramatic change in torque values stems from resonance effects on the magnitude of vibrations and resulting pressures. The magnitude of local vibrations and, hence, the local momentum flux (since velocity is the product of frequency and displacement amplitude) and pressure increase greatly near the resonance frequencies of a free-standing ring in a standing wave. These effects average out in the calculation of the total force (Eq. 11) since the total volume change due to the compressibility is very small and out-of-phase displacements tend to cancel out. Whereas the torque depends on the amplitude of local vibrations, and due to the cross-product with the position as given by Eq. 13, those effects do not cancel out. Displacement and pressure amplitudes are shown in FIG 7 to further elaborate the effects of vibrations near resonance. FIG 7a shows the displacement field for the ring with a minor radius of $a = 3.1\mu m$, for which the displacements are on the order of nanometers. Whereas in FIG 7b, for $a = 4.1\mu$, displacements are on the order of microns, about four orders of magnitude larger than displacements for $a = 3.1\mu m$ as the indicative or resonance. Similarly, FIG 7c and FIG 7d show the corresponding pressure profiles and the maximum amplitude increases four orders of magnitude in the resonating case. Furthermore, dramatic effects of resonance on acoustic torques are observed for other asymmetrical structures such as discs as well [45].

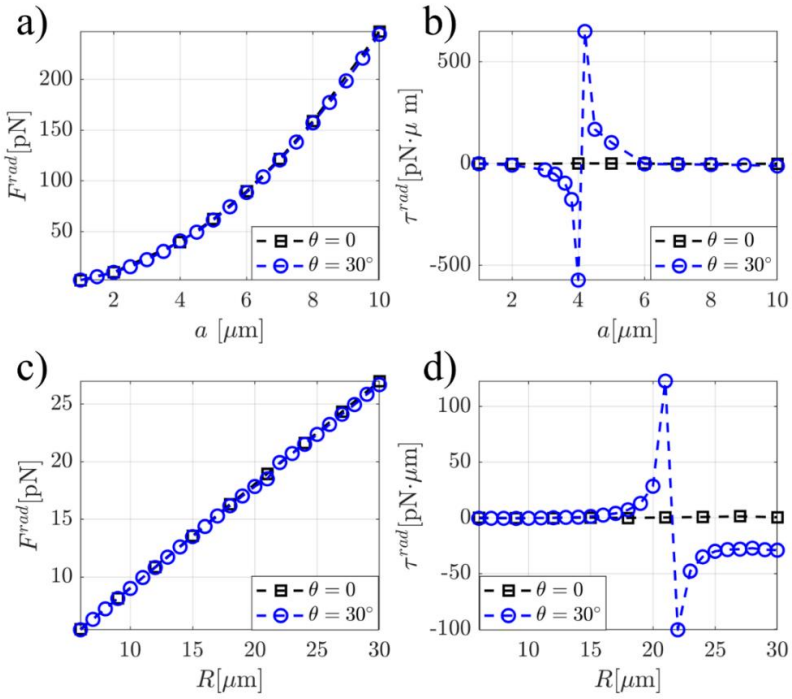

FIG 6. (a) Change of F^{rad} with respect to a, (b) change of τ^{rad} with respect to a, (c) change of F^{rad} with respect to R and (d) Change of τ^{rad} with respect to R.

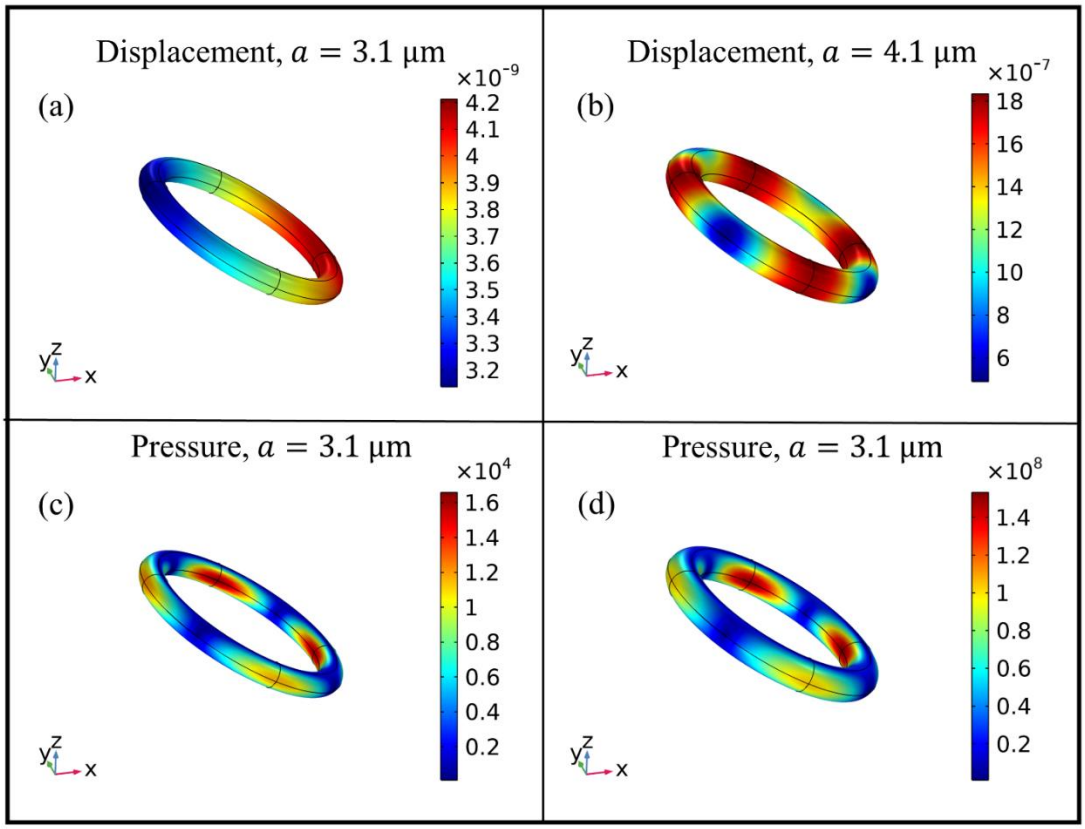

FIG 7. The displacement ((a)-(b)) and the pressure ((c)-(d)) distributions on non-resonating ((a) and (c)) and resonating ((b) and (d)) rings.

3.3 Effects of Physical Parameters

This section reports how the physical parameters affect the radiation forces and torques on a tilted ring ($\theta = 30°$). The first parameter investigated is the acoustophoretic contrast factor ϕ, defined as [13]:

$$\phi(\tilde{\kappa}, \tilde{\rho}) = \frac{1}{3}\left[\frac{5\tilde{\rho} - 2}{2\tilde{\rho} + 1} - \tilde{\kappa}\right] \tag{16}$$

where $\tilde{\rho} = \rho_p/\rho_f$ and $\tilde{\kappa} = \kappa_p/\kappa_f$ represent the ratios of densities and compressibility values of the particle to the fluid, respectively. The sensitivity analysis contains both negative and positive ϕ values which indicate whether the particle is attracted ($\phi > 0$) or repelled ($\phi < 0$) from a pressure node. F^{rad} values plotted at FIG 8a show the transition from negative (repulsive) to positive (attractive) values. The force exhibits a steeper decrease at low ϕ but as ϕ approaches 0 the rate of decrease becomes linear. On the other hand, the torque values, plotted at FIG 8b show that the torque is minimum in magnitude at $\phi \approx 0.1$. All torque values are negative, meaning that the torques tend to align the ring horizontally at all ϕ values. Lastly, we demonstrate the effect of the acoustic frequency f on forces and torques in FIG 8c and FIG 8d

respectively. The force increases linearly with respect to f while τ^{rad} increases with respect to f with a higher order dependence. According to the dimensional analysis in Appendix A, the ART is expected to scale with the square of the wavenumber, or the square of the frequency for standing waves. Moreover, there is a resonance-type behavior at $f = 4$ MHz similarly to the behavior in FIG 7. Insets in FIG 8d show the deformation modes of the vibrating ring, which are magnified by 5000 times for visual clarity (actual displacements are on the order of nanometers). At 4 MHz, amplitude of the Mises stresses increases nearly ten folds associated with the resonance between the solid ring and the standing waves in the fluid medium. A coupled eigenfrequency analysis for the deformation of the polystyrene ring and the pressure in the fluid medium shows that a deformation mode with the same shape as the one shown in FIG 8d occurs at 4.0118 MHz even though the same mode is observed at 5.221 MHz for free-standing ring. Resonance effects are also reported for torques on other nonspherical particles in standing waves, such as on discs by Garbin et. Al [45] and on helices by Caldag & Yesilyurt [12].

Finite-element (FEM) results are compared with the results of a reduced-order model called the chain-of-spheres method (CoS), which is developed for the calculation of the acoustic radiation forces and torques on slender helices for microswimming applications [12]. According to the CoS, a ring can be divided into a number of segments and each segment can be represented by an equal volume sphere, for which analytical force calculations are available. By virtue of the approach, the CoS method neglects two types of interaction forces: first, the forces that develop within the solid due to higher order modes of deformation of the ring, such as bending, extension, stretching and so on that differ from the deformation modes of a sphere, and second, the forces that develop within the fluid due to the scattered waves. Those secondary effects are intrinsically considered by the three-dimensional modeling approach in the FEM model. Therefore, discrepancies between the CoS and FEM results are used as an indication of these secondary effects.

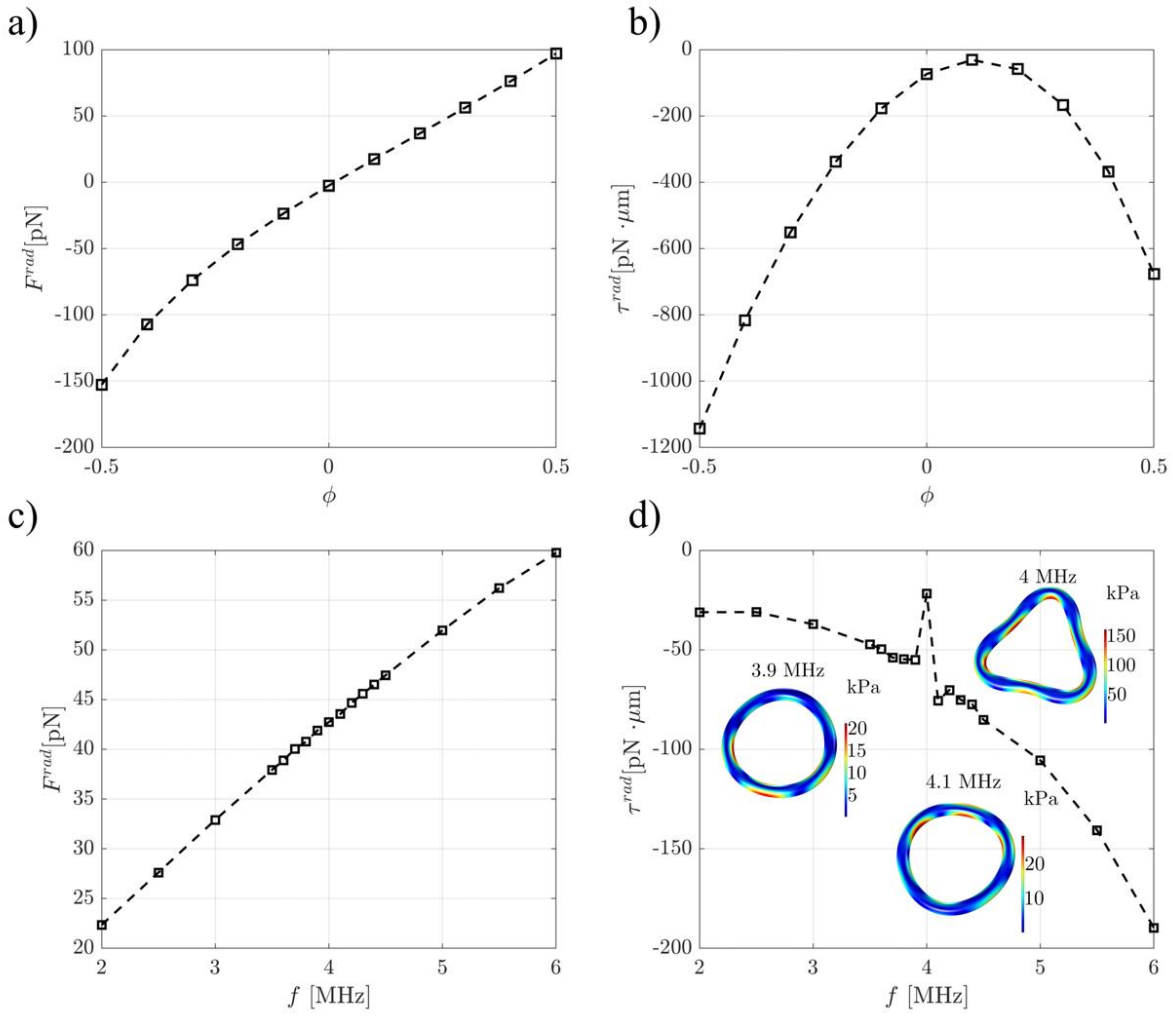

FIG 8. The change of (a) F^{rad} and (b) τ^{rad} with respect to ϕ. The change of (c) F^{rad} and (d) τ^{rad} with respect to f. Insets show the deformations (5000 times scaled-up for visual clarity) and Mises stresses in the rings.

In CoS calculations, the ring is divided into N_{sph} equal segments that are approximated by spheres having the same volume as each segment, which extends between φ_j and φ_{j+1}, where φ is the azimuthal angle and $j = 1, \dots, N_{sph} - 1$; j^{th} sphere is placed at the centroid of the j^{th} segment, which is given by:

$$\mathbf{c}_j = \frac{N_{sph}}{2\pi} \int_{\varphi_j}^{\varphi_{j+1}} \mathbf{R}_{\boldsymbol{\theta}} \mathbf{p}_r(\varphi) d\varphi \tag{17}$$

where the position vector, $\mathbf{p}_r(\varphi) = R[\cos\varphi\,, \sin\varphi\,, 0]'$, gives the centerline of the ring in the reference frame, and $\mathbf{R}_{\boldsymbol{\theta}}$ is the rotation matrix for the frame rotated by θ with the ring as shown in FIG 1. The radius of spheres is set to $a_s = \left(\frac{3\pi a^2 R}{2N_{sph}}\right)^{1/3}$ to ensure that spheres have the same volume as the segments. A simple schematic of the approach is depicted in FIG 9.

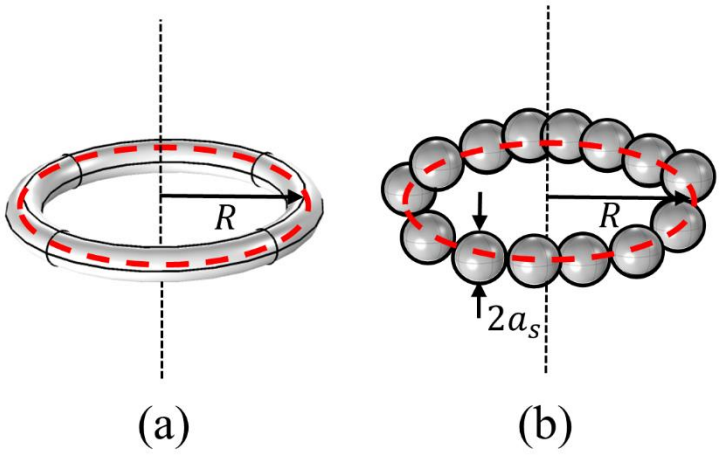

FIG 9. Application of chain-of-spheres. (a) Shows the original ring geometry, (b) shows the representation of the ring with $N_{sph} = 14$ spheres with radius a_s placed along the circle of the ring which is R away from the center of the ring. The circle is shown in red dashes.

For standing waves, Hasegawa [23] reported a simple analytical formula for the acoustic radiation force on each elastic sphere:

$$F_j^{rad} = \pi a_s^2 E Y_{st} \sin(2k\Delta z) \tag{18}$$

where $E = \frac{1}{2}\rho_0 k^2 |A|^2$ is the acoustic energy density (with A being the potential amplitude of the field), and Y_{st} is called the acoustic radiation force function [23]. Thus, the total radiation force and torque are calculated from the summations over each sphere:

$$F^{rad} = \sum_{j=1}^{N_{sph}} F_j^{rad} \tag{19}$$

$$\tau^{rad} = \sum_{j=1}^{N_{sph}} (\mathbf{c}_j - \mathbf{r}_0) \times F_j^{rad} \tag{20}$$

The reader is referred to [12] for further details on CoS and reference [23] for the calculation of the acoustic radiation force in a standing field.

Comparisons are carried out with respect to varying Δz for a tilted ring with $\theta = 30°$ for polystyrene, copper and aluminum rings and the results are shown in FIG 10. In CoS calculations, first a convergence study is carried out and the number of segments is set to $N_{sph} = 25$ as a sufficiently large value to control the error due to the segmentation of the ring. For the polystyrene and copper rings, F^{rad} values exhibit a good agreement with the FEM results (FIG 10a and FIG 10c) for all Δz; agreement is much better for polystyrene than copper, for which a

maximum of 5% relative error is observed. Whereas the agreement is poor for the aluminum ring for F^{rad}, as depicted in FIG 10e. Similarly, torque values, τ^{rad}, are plotted in FIG 10b, FIG 10d and FIG 10f, where we observe a significant discrepancy between the FEM and the CoS results for polystyrene and copper rings and the discrepancy is more pronounced for the copper ring. Interestingly, despite the deviations between the FEM and the CoS results for F^{rad} computation in the aluminum ring, the torque values exhibit a very good agreement.

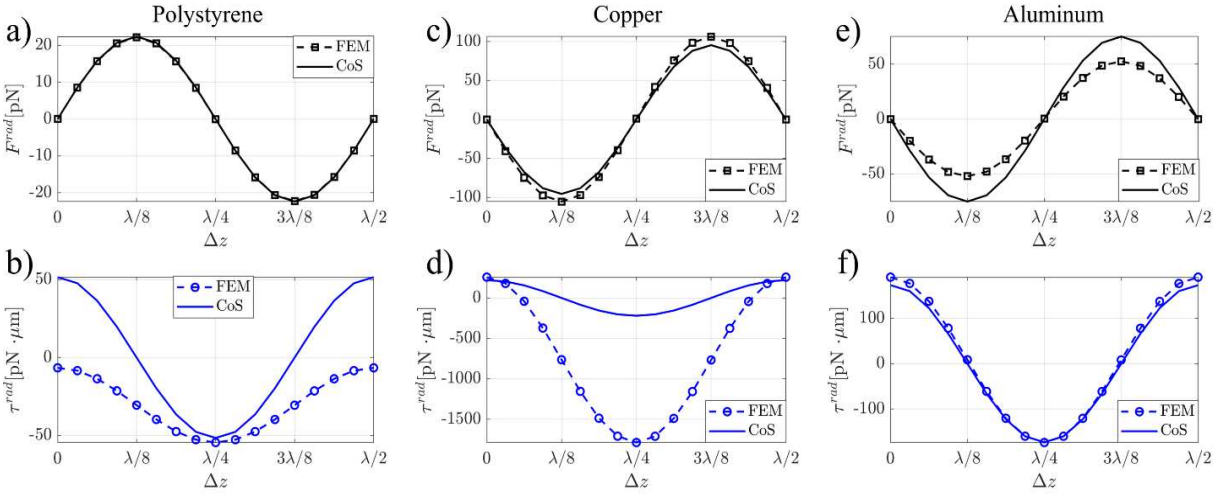

FIG 10. Comparison of the radiation forces ((a), (c) and (e)) and torques ((b), (d) and (f)) obtained from the FEM model and with the CoS approach. (a) and (b) show the results for polystyrene, (c) and (d) show the results for copper and (e) and (f) show the results for aluminum.

To elucidate on the discrepancies in torque computations, we first confirm that the force and torque contributions from each sphere in the CoS model match with the values evaluated from the FEM model by simulating individual ring segments in separate FEM simulations. This is not shown in the plots separately as it will be a repetition of the CoS results in FIG 10a and FIG 10b. This step indicates that the basic premise of the CoS approach holds, i.e., individual segments of the ring can be considered as spheres and both the force and torque computations are consistent. Next, we compare the radiation forces on rings that are composed of 10 toroidal segments using the FEM model. FIG 11a shows the toroidal segments forming the ring with a small gap of 2° between them, this gap size is kept negligibly small with minimal ramifications on the convergence of FEM simulations. Acoustic radiation forces (ARF) are calculated for segmented polystyrene, copper and aluminum rings at the baseline configuration in Table I with $\Delta z = \lambda/8$ and $\theta = 30°$. Segments are placed one by one in their original position according to the numbering given in Fig. 11a. Thus, each segment's position is obtained from the complete ring placed at the same $\Delta z = \lambda/8$ and $\theta = 30°$ to keep the position of each segment the same. Forces on segments are calculated for three different arrangements: (i) for each single segment

individually placed in the acoustic field one at a time; (ii) for all detached segments that form the ring shape as shown in FIG 11a; and (iii) for the complete ring composed of segments connected to each other. ARF values are shown in FIG 11b-d for polystyrene, copper, and aluminum rings respectively. For the polystyrene ring, it is observed that force values vary negligibly (less than .05 pN) between the segments either placed one at a time individually or altogether as shown in FIG 11b. This result indicates clearly that self-scattering between the segments does not play an important role on local forces whereas the elastic behavior of the whole slender structure does for which the maximum deviation takes place at segment 6 as high as 9.9 pN. For the copper ring, we see the force values vary slightly between 9.05 and 10.57 pN for individual segments placed one at a time (black circles in FIG 11c), small deviations are due to numerical error in calculating stresses around the sharp edges of segments, further improvements to the mesh up to 3M dof (exceeding a memory requirement of 140 GB) do not alter the results significantly. Forces on the detached segments, when they are placed in the acoustic field together, differ significantly than the forces on individual segments, up to 7.5 pN for the first segment. Moreover, for segments 3-8, forces on the detached segments (red stars) are very close to the forces on the corresponding segments in the ring (blue squares), as the difference is within 1.8 pN for these segments. This result indicates that, scattering of waves between the segments have an important role on the ARF. Lastly, for the aluminum ring, we observe that the ARF behavior is closer to polystyrene than copper as the deviation between the forces on singled and detached segments is less than 2.8 pN, and overall, smaller than the deviation between the local forces on detached segments and the complete ring segments, which reaches up to 5.8 pN for the 6^{th} segment. The conclusion is that decomposing the ring into detached segments changes the local forces without affecting the total net force. Hence, the chain-of-spheres approach fails at evaluating the torques properly whereas it gives close results in aggregation to the FEM results for the whole ring. The CoS approach needs to be improved by including the links between the spheres to capture the bending moments and the effects of the scattered acoustic field to check the importance of those effects.

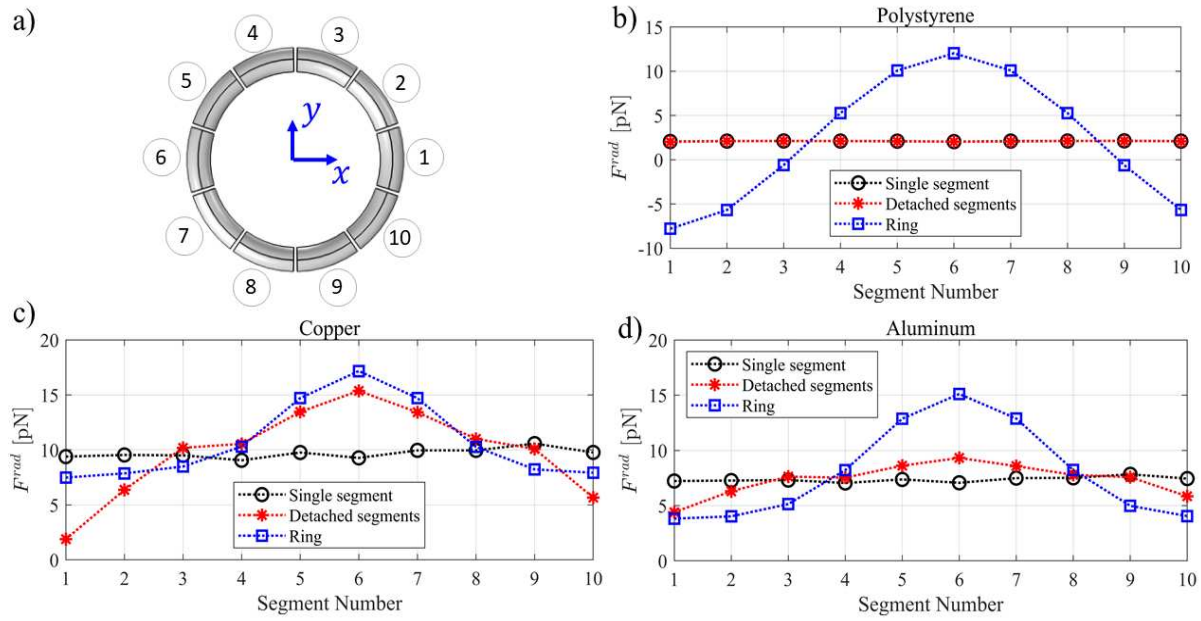

FIG 11. (a) The depiction of the ring decomposed into segments; local acoustic radiation forces (ARF) on each segment of polystyrene (b), copper (c) and aluminum (d) rings. ARF on each individual segment placed in the acoustic field without others is shown with black circles; forces on the detached segments forming a ring (see the picture in (a)) is shown with red stars; and the forces on the complete ring composed of segments in contact are shown with blue squares.

4. Conclusions

This study reports the effects of minor and major radii, position, orientation and physical properties on the acoustic radiation forces (ART) and torques (ART) on a micro ring placed in a standing acoustic wave in water based on a finite-element model (FEM). The ARF is proportional to the volume of the ring and reaches to maximum when the ring is $\lambda/8$ away from the pressure node, similarly to the force on spherical particles. On the other hand, the ART tends to align the rings with respect to plane waves and hits its maximum amplitude at the pressure anti-node. The stable alignment of the ring could be horizontal ($\tau^{rad} < 0$ for $\theta > 0$) or vertical ($\tau^{rad} > 0$ for $0 < \theta < \pi/2$) depending on geometric and physical parameters. For $\Delta z = 0$, the torque is negative for rings with orientations $\theta < \sim 35°$ and vertical otherwise, whereas the alignment is always horizontal for $\Delta z = \lambda/8$. Since the torque depends on the local force distribution, in certain configurations very large torque values are observed because of the resonant behavior of the ring, which is not manifest in force results.

Moreover, the ARF on a ring is sensitive to the acoustophoretic contrast factor and attractive ($F^{rad} < 0$) for $\phi < 0$ and repulsive otherwise. Whereas the torque does not change sign with ϕ but hits a minimum in magnitude at a small positive contrast factor for the configurations studied here. Furthermore, we compared the FEM results with a reduced-order-model called chain-of-spheres model (CoS), which predicts the ARF very well especially for

soft materials, but the torque predictions are not accurate because of the contributions from local forces are more important and as the approach does not include self-scattering effects. The importance of the local forces is demonstrated by separate FEM simulations for a segmented ring. It is observed that for the polystyrene ring, self-scattering does not contribute to local forces, which is dominated by the elastic behavior of the solid. On the other hand, for the copper ring, self-scattering plays a very important role on the local force. Overall findings of this study are expected to be useful for acoustophoretic manipulation and reorientation of ring-like micro filaments and other non-spherical slender bodies. Our analysis shows that self-scattering of acoustic waves and bending of the slender rods play an important role on the overall acoustic torque on the structure, which may be helpful to determine the orientation of the structure at equilibrium as well as orientational instabilities under resonance. The predictions can be utilized in controlled rotation and manipulation of such structures in a non-invasive manner, an attribute particularly useful for manipulating the orientation of a biological sample for imaging purposes. As acoustic fields are widely used in biomedicine, we anticipate that such applications can be realized effectively. Lastly, the chain-of-spheres approach is very useful determining the acoustic radiation forces, but improvements are necessary for accurate torque predictions via including self-scattering of the acoustic waves and internal stresses.

Appendix A

Appendix A. Dimensional Analysis

Consider a ring of minor radius, a, major radius, R, density, ρ_p, speed of sound, c_p, is placed in a standing acoustic wave of pressure amplitude, p_a, frequency, f, in a fluid of density, ρ_0 and speed of sound, c_0. The distance of the ring from the pressure node is Δz and its orientation with respect to the x-y plane is given by θ as shown in Fig. A1. Among the ten variables, a, ρ_0 and c_0 can be picked as representatives of length, mass, and time dimensions. Then, the dimensionless Π numbers for the remaining six variables are:

$$\Pi_{\{R,z,\rho_p,c_p,p_a,f\}} = \left\{ \frac{R}{a}, \frac{\Delta z}{a}, \frac{\rho_p}{\rho_0}, \frac{c_p}{c_0}, \frac{p_a}{\rho_0 c_0^2}, \frac{af}{c_0} \right\} \tag{A1}$$

The derived variables $\lambda = \frac{c_0}{f}$ and $k = \frac{2\pi}{\lambda}$ are not included in this list since they are already given by the combination of other variables already in the list, hence instead of Π_f, we can use $\Pi_\lambda = \lambda/a$ or $\Pi_k = ka$ when it is convenient.

By nondimensionalizing the pressure terms by $\rho_0 c_0^2$, we can obtain dimensionless groups for the acoustic radiation force and torque as:

$$\Pi_{\{F,\tau\}} = \left\{ \frac{F_{rad}}{\rho_0 c_0^2 a^2}, \frac{\tau_{rad}}{\rho_0 c_0^2 a^3} \right\} \tag{A2}$$

Thus the Π terms for the force and torque are functions of the six terms given in Eq. (A1) plus angle θ.

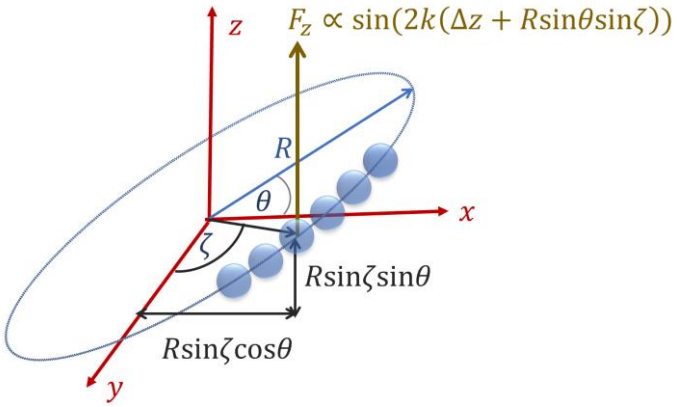

Fig. A1. Representation of the local acoustic radiation force on a tilted ring, which is approximated by a chain of spherical particles.

To obtain the dimensionless form of the force we can resort to the analytical solution for the spherical particle in a standing cosine wave reported by Yosioka and Kawasima [20] and modified by Settnes & Bruus [14]:

$$F_{rad} = \frac{\pi a^3 p_a^2 \phi k}{\rho_0 c_0^2} \sin(2k\Delta z) \;\Rightarrow\; \Pi_F = \pi \Pi_{p_a}^2 \Pi_k \sin(2\Pi_{\Delta z}\Pi_k)\, \phi\left(\Pi_{\rho_p}, \Pi_{c_p}\right) \tag{A3}$$

where ϕ is the acoustophoretic contrast factor given by Eq. 16. This expression is more convenient in showing the parametric dependences than the one used in Eq. (18) but less accurate.

For the effect of θ on the force, we assume that the ring consists of a chain of spherical particles as shown in Fig. A1. To estimate the total force on the tilted ring we estimate the integral of the sine term over the toroidal angle ζ as shown in A3 as follows:

$$\int_{-\pi}^{\pi} \sin\big(2k(\Delta z + R\sin\theta\sin\zeta)\big)\, d\zeta$$

$$= \int_{0}^{\pi} \sin\big(2k(\Delta z + R\sin\theta\sin\zeta)\big) + \sin\big(2k(\Delta z - R\sin\theta\sin\zeta)\big)\, d\zeta$$

$$= \int_{0}^{\pi} 2\cos(2Rk\,\sin\zeta\,\sin\theta)\sin(2k\Delta z)\;\, d\zeta$$

$$= 2\pi\sin(2k\Delta z)\, J_0\,(2Rk\sin\theta) \tag{A5}$$

Hence the θ dependence of the force on the ring is expressed with the zeroth order Bessel function of the first kind $J_0(2Rk\sin\theta)$. From the definition of the wave number, $k = \frac{2\pi}{\lambda}$, we have $2Rksin\theta = 4\pi\sin\theta R/\lambda$. Therefore, in the case of $R \ll \lambda$, this effect is negligible since $J_0(x) \to 1$ as $x \to 0$. Thus, the orientation angle of the ring has a minor effect on the ARF for small rings.

Using the analytical solution for the sphere given by Eq. (A3) and the sketch of the ring shown in Fig. A1, we postulate that the acoustic radiation force scales with the volume of the particle, thus the a^3 term for the spherical particle should be replaced by a^2R. However, the pre-factor can be different in that case, therefore the nondimensional force would be proportional to other dimensionless quantities as

$$\Pi_F \propto \Pi_R\Pi_{p_a}^2\Pi_k \sin(2\Pi_{\Delta z}\Pi_k)\, \phi\left(\Pi_{\rho_p}, \Pi_{c_p}\right) J_0(4\Pi_R\Pi_k \sin\theta) \tag{A6}$$

To obtain the effect of orientation on the torque we integrate the torque due to each spherical particle over the toroidal angle ζ as shown in Fig. A1

$$\int_{-\pi}^{\pi} \sin\big(2k(\Delta z + R\sin\theta\sin\zeta)\big)\, R\cos\theta\sin\zeta\; d\zeta$$

However, this integral cannot be obtained in the closed form. Nonetheless, with a simplistic approach that the ring consists of two spherical particles which represent the opposing segments placed at $\zeta = \pm\pi/2$, we can obtain an approximation for the orientation effect on the torque:

$$T \propto R\cos\theta\, \left(F_{\zeta=\frac{\pi}{2}} - F_{\zeta=-\frac{\pi}{2}}\right) = R\cos\theta\big[\sin\big(2k(\Delta z + R\sin\theta)\big) - \sin\big(2k(\Delta z - R\sin\theta)\big)\big] \tag{A7}$$

The sine terms in the square brackets can be simplified as:

$$\sin\big(2k(\Delta z + R\sin\theta)\big) - \sin\big(2k(\Delta z - R\sin\theta)\big) = \cos(2k\Delta z)\sin(2kR\sin\theta)$$

The $\sin(2kR\,\sin\theta) = \sin(4\pi R\sin\theta/\lambda)$ term represents the effect of the orientation on the torque. Thus, in the case of $R \ll \lambda$ the net torque scales with $kR\sin\theta$. Therefore, the

dimensionless acoustic torque for small rings is cast in the following form with a cosine dependence on the position and sinusoidal dependence on the orientation:

$$\Pi_T \propto \Pi_R^3 \Pi_{p_a}^2 \Pi_k^2 \cos(2\Pi_{\Delta z}\Pi_k) \sin\theta \; \phi\left(\Pi_{\rho_p}, \Pi_{c_p}\right) \tag{A8}$$

However, this expression does not have the bending and resonance effects, which dominate the time-harmonic torque on the ring in a standing wave. The acoustophoretic coefficient, $\phi(\Pi_{\rho_p}, \Pi_{c_p})$, accounts only for the compression of spherical particles here, and not suitable for time-harmonic deformation of a slender body.

References

[1] F. O. Schmitt, "Ultrasonic micromanipulation," Protoplasma, vol. 7, no. 1, pp. 332-340, 1929.

[2] X. Peng, W. He, F. Xin, G. M. Genin, and T. J. Lu, "The acoustic radiation force of a focused ultrasound beam on a suspended eukaryotic cell," Ultrasonics, vol. 108, p. 106205, 2020/12/01/ 2020, doi: https://doi.org/10.1016/j.ultras.2020.106205.

[3] W. T. Coakley, D. W. Bardsley, M. A. Grundy, F. Zamani, and D. J. Clarke, "Cell manipulation in ultrasonic standing wave fields," Journal of Chemical Technology & Biotechnology, vol. 44, no. 1, pp. 43-62, 1989.

[4] A. Haake, A. Neild, G. Radziwill, and J. Dual, "Positioning, displacement, and localization of cells using ultrasonic forces," Biotechnology and bioengineering, vol. 92, no. 1, pp. 8-14, 2005.

[5] S. Deshmukh, Z. Brzozka, T. Laurell, and P. Augustsson, "Acoustic radiation forces at liquid interfaces impact the performance of acoustophoresis," Lab on a Chip, vol. 14, no. 17, pp. 3394-3400, 2014.

[6] Li, Yuyang, Xiaoming Liu, Qiang Huang, Aaron T. Ohta, and Tatsuo Arai. "Bubbles in microfluidics: an all-purpose tool for micromanipulation." Lab on a Chip 21, no. 6 (2021): 1016-1035.

[7] P. Glynne-Jones, R. J. Boltryk, M. Hill, N. R. Harris, and P. Baclet, "Robust acoustic particle manipulation: A thin-reflector design for moving particles to a surface," The Journal of the Acoustical Society of America, vol. 126, no. 3, pp. EL75-EL79, 2009, doi: 10.1121/1.3186800.

[8] Leao-Neto, Jose P., et al. "Acoustic radiation force and torque on spheroidal particles in an ideal cylindrical chamber." The Journal of the Acoustical Society of America 149.1 (2021): 285-295.

[9] Gong, Zhixiong, and Michael Baudoin. "Three-dimensional trapping and dynamic axial manipulation with frequency-tuned spiraling acoustical tweezers: a theoretical study." Physical Review Applied 16.2 (2021): 024034.

[10] G. Thalhammer, R. Steiger, M. Meinschad, M. Hill, S. Bernet, and M. Ritsch-Marte, "Combined acoustic and optical trapping," Biomed. Opt. Express, vol. 2, no. 10, pp. 2859-2870, 2011/10/01 2011, doi: 10.1364/BOE.2.002859.

[11] M. Kvåle Løvmo, B. Pressl, G. Thalhammer, and M. Ritsch-Marte, "Controlled orientation and sustained rotation of biological samples in a sono-optical microfluidic device," Lab on a Chip, 10.1039/D0LC01261K vol. 21, no. 8, pp. 1563-1578, 2021, doi: 10.1039/D0LC01261K.

[12] H. O. Caldag and S. Yesilyurt, "Acoustic radiation forces on magnetically actuated helical swimmers," Physics of Fluids, vol. 32, no. 9, p. 092012, 2020, doi: 10.1063/5.0020930.

[13] H. Bruus, "Acoustofluidics 7: The acoustic radiation force on small particles," Lab on a Chip, vol. 12, no. 6, pp. 1014-1021, 2012.

[14] M. Settnes and H. Bruus, "Forces acting on a small particle in an acoustical field in a viscous fluid," Physical Review E, vol. 85, no. 1, p. 016327, 2012.

[15] T. Baasch, A. Pavlic, and J. Dual, "Acoustic radiation force acting on a heavy particle in a standing wave can be dominated by the acoustic microstreaming," Physical Review E, vol. 100, no. 6, p. 061102, 2019.

[16] P. Glynne-Jones, P. P. Mishra, R. J. Boltryk, and M. Hill, "Efficient finite element modeling of radiation forces on elastic particles of arbitrary size and geometry," The Journal of the Acoustical Society of America, vol. 133, no. 4, pp. 1885-1893, 2013.

[17] A. Doinikov, "Acoustic radiation pressure on a rigid sphere in a viscous fluid," Proceedings of the Royal Society of London. Series A: Mathematical and Physical Sciences, vol. 447, no. 1931, pp. 447-466, 1994.

[18] A. A. Doinikov, "Acoustic radiation pressure on a compressible sphere in a viscous fluid," Journal of Fluid Mechanics, vol. 267, pp. 1-22, 1994.

[19] L. V. King, "On the acoustic radiation pressure on spheres," Proceedings of the Royal Society of London. Series A-Mathematical and Physical Sciences, vol. 147, no. 861, pp. 212-240, 1934.

[20] K. Yosioka and Y. Kawasima, "Acoustic radiation pressure on a compressible sphere," Acta Acustica united with Acustica, vol. 5, no. 3, pp. 167-173, 1955.

[21] L. P. Gor'kov, "On the Forces Acting on a Small Particle in an Acoustical Field in an Ideal Fluid," Soviet Physics Doklady, vol. 6, p. 773, March 01, 1962 1962. [Online]. Available: https://ui.adsabs.harvard.edu/abs/1962SPhD....6..773G.

[22] T. Hasegawa and K. Yosioka, "Acoustic-Radiation Force on a Solid Elastic Sphere," The Journal of the Acoustical Society of America, vol. 46, no. 5B, pp. 1139-1143, 1969, doi: 10.1121/1.1911832.

[23] T. Hasegawa, "Acoustic radiation force on a sphere in a quasistationary wave field—theory," The Journal of the Acoustical Society of America, vol. 65, no. 1, pp. 32-40, 1979, doi: 10.1121/1.382263.

[24] J. T. Karlsen and H. Bruus, "Forces acting on a small particle in an acoustical field in a thermoviscous fluid," (in eng), Phys Rev E Stat Nonlin Soft Matter Phys, vol. 92, no. 4, p. 043010, Oct 2015, doi: 10.1103/PhysRevE.92.043010.

[25] A. A. Doinikov, "Acoustic radiation force on a spherical particle in a viscous heat-conducting fluid. I. General formula," The Journal of the Acoustical Society of America, vol. 101, no. 2, pp. 713-721, 1997, doi: 10.1121/1.418035.

[26] A. A. Doinikov, "Acoustic radiation force on a spherical particle in a viscous heat-conducting fluid. II. Force on a rigid sphere," The Journal of the Acoustical Society of America, vol. 101, no. 2, pp. 722-730, 1997, doi: 10.1121/1.418036.

[27] A. A. Doinikov, "Acoustic radiation force on a spherical particle in a viscous heat-conducting fluid. III. Force on a liquid drop," The Journal of the Acoustical Society of America, vol. 101, no. 2, pp. 731-740, 1997, doi: 10.1121/1.417961.

[28] Q. Wang, A. Riaud, J. Zhou, Z. Gong, and M. Baudoin, "Acoustic Radiation Force on Small Spheres Due to Transient Acoustic Fields," Physical Review Applied, vol. 15, no. 4, p. 044034, 04/21/ 2021, doi: 10.1103/PhysRevApplied.15.044034.

[29] K. A. Johnson et al., "Experimental verification of theoretical equations for acoustic radiation force on compressible spherical particles in traveling waves," Physical Review E, vol. 93, no. 5, p. 053109, 05/17/ 2016, doi: 10.1103/PhysRevE.93.053109.

[30] G. T. Silva and B. W. Drinkwater, "Acoustic radiation force exerted on a small spheroidal rigid particle by a beam of arbitrary wavefront: Examples of traveling and standing plane waves," The Journal of the Acoustical Society of America, vol. 144, no. 5, pp. EL453-EL459, 2018, doi: 10.1121/1.5080529.

[31] R. Wu, K. Cheng, X. Liu, J. Liu, X. Gong, and Y. Li, "Study of axial acoustic radiation force on a sphere in a Gaussian quasi-standing field," Wave Motion, vol. 62, pp. 63-74, 2016/04/01/ 2016, doi: https://doi.org/10.1016/j.wavemoti.2015.12.005.

[32] F. G. Mitri, "Acoustic radiation force on a sphere in standing and quasi-standing zero-order Bessel beam tweezers," Annals of Physics, vol. 323, no. 7, pp. 1604-1620, 2008/07/01/ 2008, doi: https://doi.org/10.1016/j.aop.2008.01.011.

[33] L. V. King, “On the acoustic radiation pressure on circular discs: Inertia and diffraction corrections,” Proc. R. Soc. London Ser. A 153, 1–16 (1935).

[34] W. J. Xie and B. Wei, "Dynamics of acoustically levitated disk samples," Physical Review E, vol. 70, no. 4, p. 046611, 10/28/ 2004, doi: 10.1103/PhysRevE.70.046611.

[35] W. T. Shi and R. E. Apfel, “Deformation and position of acoustically levitated liquid drops,” J. Acoust. Soc. Am. 99, 1977–1984 (1996).

[36] F. Cai, L. Meng, C. Jiang, Y. Pan, and H. Zheng, “Computation of the acoustic radiation force using the finite-difference time-domain method,” J. Acoust. Soc. Am. 128, 1617–1622 (2010).

[37] D. Haydock, “Lattice Boltzmann simulations of the time-averaged forces on a cylinder in a sound field,” J. Phys. A 38, 3265–3277 (2005).

[38] F. G. Mitri, “Theoretical calculation of the modulated acoustic radiation force on spheres and cylinders in a standing plane wave-field,” Physica D 212, 66–81 (2005).

[39] J. Wang and J. Dual, "Numerical simulations for the time-averaged acoustic forces acting on rigid cylinders in ideal and viscous fluids," Journal of Physics A: Mathematical and Theoretical, vol. 42, no. 28, p. 285502, 2009/06/24 2009, doi: 10.1088/1751-8113/42/28/285502.

[40] P. L. Marston, W. Wei, and D. B. Thiessen, in Innovations in Nonlinear Acoustics, edited by A. A. Atchley, V. W. Sparrow, and R. M. Keolian (AIP, Melville, NY, 2006), Vol. 838, pp. 495–499.

[41] F. G. Mitri, "Theoretical and experimental determination of the acoustic radiation force acting on an elastic cylinder in a plane progressive wave—far-field derivation approach," New Journal of Physics, vol. 8, no. 8, pp. 138-138, 2006/08/18 2006, doi: 10.1088/1367-2630/8/8/138.

[42] A. Grinenko, P. D. Wilcox, C. R. Courtney, and B. W. Drinkwater, "Acoustic radiation force analysis using finite difference time domain method," (in eng), J Acoust Soc Am, vol. 131, no. 5, pp. 3664-70, May 2012, doi: 10.1121/1.3699204.

[43] F. B. Wijaya and K. M. Lim, "Boundary Element and Meshless Methods on Acoustics and Vibrations : Paper ICA 2016-181 Boundary element method for acoustic radiation force and torque acting on non-spherical particles," 2016.

[44] F. B. Wijaya and K. M. Lim, "Numerical calculation of acoustic radiation force and torque on non-spherical particles in Bessel beams," Proceedings of Meetings on Acoustics, vol. 26, no. 1, p. 045002, 2016, doi: 10.1121/2.0000251.

[45] A. Garbin, I. Leibacher, P. Hahn, H. L. Ferrand, A. Studart, and J. Dual, "Acoustophoresis of disk-shaped microparticles: A numerical and experimental study of acoustic radiation forces and torques," *The Journal of the Acoustical Society of America,* vol. 138, no. 5, pp. 2759-2769, 2015, doi: 10.1121/1.4932589.

[46] E.B Lima, J.P. Leão-Neto, A.S. Marques, G.C. Silva, J.H. L & G.T. Silva, Nonlinear interaction of acoustic waves with a spheroidal particle: Radiation force and torque effects. Physical Review Applied, 13(6), 064048 (2020).

[47] Nguyen, Tan Dai, Van Thai Tran, Yong Qing Fu, and Hejun Du. "Patterning and manipulating microparticles into a three-dimensional matrix using standing surface acoustic waves." Applied Physics Letters 112, no. 21 (2018): 213507.

[48] N.C. Lim, and S.E. Jackson, “Molecular knots in biology and chemistry.” Journal of Physics: Condensed Matter, 27(35), p.354101 (2015).

[49] Li, M.H., Chen, C.Y., Li, C.S., Chin, C.H. and Li, S.S., 2014. Design and characterization of a dual-mode CMOS-MEMS resonator for TCF manipulation. Journal of Microelectromechanical Systems, 24(2), pp.446-457.

[50] T. J. Steiner, J. E. Castro, L. Chang, Q. Dang, W. Xie, J. Norman, ... & G. Moody. "Ultrabright Entangled-Photon-Pair Generation from an Al Ga As-On-Insulator Microring Resonator," PRX Quantum, 2(1), 010337 (2021).

[51] X. Hu, J. Zhu, Y. Zuo, D. Yang, J. Zhang, Y. Cheng, Y. Yang. "Versatile biomimetic array assembly by phase modulation of coherent acoustic waves", Lab on a Chip 20 (2020) 3515-3523

[52] M.D. Haslam, B. Raeymaekers. "Aligning carbon nanotubes using bulk acoustic waves to reinforce polymer composites", Composites Part B: Engineering 60 (2014) 91-97.

[53] A. A. Doinikov, "Acoustic radiation forces: Classical theory and recent advances," Recent research developments in acoustics, vol. 1, pp. 39-67, 2003.

[54] F. G. Mitri, "Transition from progressive to quasi-standing waves behavior of the radiation force of acoustic waves—Example of a high-order Bessel beam on a rigid sphere," Journal of Sound and Vibration, vol. 329, no. 16, pp. 3319-3324, 2010/08/02/ 2010, doi: https://doi.org/10.1016/j.jsv.2010.02.025.

[55] COMSOL Multiphysics® v. 5.6. COMSOL AB, Stockholm, Sweden. 2020.

[56] D. Givoli, and B, Neta. "High-order non-reflecting boundary scheme for time-dependent waves." Journal of Computational Physics 186(1), 24-46, 2003.

[57] Łodygowski, T. and Sumelka, W., 2006. Limitations in application of finite element method in acoustic numerical simulation. Journal of Theoretical and Applied Mechanics, 44(4), pp.849-865